Vol. 7: 151–168, 1996 | CLIMATE RESEARCH Clim Res | Published November 29

Verification of statistical-dynamical downscaling in the Alpine region

Ursula Fuentes*, Dietrich Heimann

DLR, Institut für Physik der Atmosphäre, Oberpfaffenhofen, D-82234 Weßling, Germany

ABSTRACT: A statistical-dynamical downscaling procedure for global climate simulations is verified for the greater Alpine region. This procedure links global and regional model simulations using frequencies of large-scale weather types in order to derive the regional climate corresponding to a given global climate. The results from multi-year global simulations or large-scale analyses are classified into a set of large-scale weather types. Regional model simulations are carried out once for each class. The model output fields are weighted with the frequencies of the corresponding weather type to give the regional climate. As downscaling procedures transmit errors in the global climate simulation to the regional scale, the verification of the statistical-dynamical procedure is based on large-scale observational data, in our case a decade of daily ECMWF (European Centre for Medium Range Weather Forecasts) analyses. The downscaled results are compared with local observations for the same decade. The verification shows that the downscaling procedure is able to reproduce climatological features of the observed regional distributions of wind and temperature. However, the downscaled regional distribution of precipitation exhibits major deficiencies. Possible reasons are discussed and further improvements of the statistical-dynamical downscaling procedure are previewed.

KEY WORDS: Regional climate · Alps · Downscaling Verification Weather-type classification · Mesoscale model simulations

1. INTRODUCTION

The horizontal resolution of transient climatological simulations with general circulation models (GCMs[1]) is presently limited to an order of some 250 km. Hence, GCMs are still unable to account for mesoscale modifications of large-scale fields in regions with complex topography. The horizontal extension of orographically disturbed currents (flow over and around mountains) and thermally induced circulation systems (valley wind systems, land-sea breezes, etc.) is far beyond the current resolution of GCMs. Therefore, results of GCMs cannot be directly used for assessing the effects of possible climate changes in regions where mesoscale features are of climatological importance.

In these cases special procedures are needed which deduce regional-scale parameters from large-scale climate simulations. Such procedures are known as 'downscaling' or 'regionalization' methods. They are generally based on a coupling of large-scale and regional-scale distributions of meteorological parameters, assuming the existence of a functional relationship between both scales.

Three alternative downscaling approaches are presently discussed:

Statistical-empirical methods use regional and global observations and derive statistical relations between regional-scale anomalies and corresponding anomalies on a scale large enough to be resolved by GCMs (von Storch et al. 1993, Zorita et al. 1995).

Dynamical or nesting methods provide a regional fine-mesh model that is nested in a GCM for a certain region. The regional model is time-dependently driven by the global model at its boundaries. Since the computational expense is large, the nesting method has

*E-mail: ursula.fuentes@dlr.de

[1] In this paper we use the abbreviation GCM to mean general circulation models that are used in long-term (several decades) climatological mode

mainly been applied to short periods of a few months (Giorgi 1990) or a few years (Giorgi et al. 1994) so far. Only recently has a 10 yr period been simulated (Jones et al. 1995) on a 50 km grid. An alternative dynamical approach is the use of a global model with varying horizontal resolution (Déqué & Piedelievre 1995).

Statistical-dynamical downscaling links global and regional model simulations through statistics derived for large-scale weather types. The regional simulations are initialized using representative vertical profiles for each weather type and then run for a short period without lateral forcing by the global model (Frey-Buness et al. 1995).

Each method has its advantages and shortcomings. With regard to the applicability of downscaling procedures to climate-impact studies, the statistical-dynamical approach combines advantages of the other 2 methods. As in dynamical downscaling, a regional model is used, and as in statistical-empirical downscaling, the computational effort does not depend on the length of the period to be downscaled. In contrast to statistical-empirical methods, statistical-dynamical downscaling does not depend on the availability of long-term observational time series. Moreover, it need not assume that statistical relationships derived for an observed climate still hold good for a scenario. Of course, these advantages do not imply that statistical-dynamical downscaling necessarily yields better results.

Statistical-dynamical downscaling consists of 3 steps which are briefly sketched below and described in some detail in Section 2. Refer to Frey-Buness et al. (1995) for further details.

(1) A multi-year time series from a GCM simulation is classified into an adequate amount of large-scale weather types characteristic for the region of interest. These weather types are defined on a scale which is well resolved by the GCM. The frequency of the weather types is used as the probability of their occurrence in the climate simulated by the GCM.

(2) Regional model simulations are carried out once for each weather type. The regional model calculates the mesoscale deviations from the large-scale state due to the impact of the regional topography. The model domain is situated within the area in which the frequencies of the large-scale weather types are derived.

(3) The regional model output is weighted with the respective frequencies of the weather types and then is statistically evaluated to yield regional distributions of climatological parameters (mean values, variances or frequency distributions) corresponding to the global climate represented by the GCM data.

Of course, statistical-dynamical downscaling has shortcomings. On the one hand, there are limitations intrinsic to this procedure. For example, the spatial resolution of the resulting regional distributions is limited by the resolution of the regional model. Obviously, this limitation equally applies to dynamical downscaling. Another inevitable limitation is the reduced reproduction of temporal variability, due to the representation of the whole variety of weather phenomena by a limited number of weather types. As a consequence, statistical-dynamical downscaling is not suited for assessing extreme events unless the method is combined with additional statistical tools.

Other limitations are not intrinsic to statistical-dynamical downscaling but are the consequence of the present setup. Due to the homogeneity and stationarity of the prescribed large-scale fields, transient features are neither permitted to enter the regional model domain (e.g. fronts) nor allowed to develop inside the domain (e.g. lee cyclones). This simplification implies a reduction of the variability of regional parameters. The remaining variability is caused by the variety of large-scale weather types and by internal variations due to thermally driven circulations (e.g. sea breeze, mountain wind systems).

Egger (1995) has proposed tests for estimating the influence of inhomogeneity and nonstationarity of the prescribed large-scale fields on the downscaling results. He showed that the statistical-dynamical method in its present form works well, provided that the large-scale fields are not dominated by transient inhomogeneities.

While Egger based his conclusions on the impact of a synthetic large-scale climate on a simplified orography, we verified our downscaling procedure by applying it to the present-day climate and to the realistic Alpine topography. A prototype application of the procedure to the greater Alpine region has already been presented by Frey-Buness et al. (1995). It was based on a GCM control run (i.e. a simulation of the present-day climate) using the ECHAM3 model in T42 resolution (Roeckner et al. 1992).

Using GCM results as large-scale input means that errors of the GCM are transmitted to the regional scale for any downscaling procedure. In this case, specific verification of the downscaling method is not possible, since it is not clear whether discrepancies between downscaled and observed climatological parameters originate from the GCM or instead from the downscaling procedure itself. Therefore, the verification of a downscaling procedure should be based on 'perfect' large-scale data that cover exactly the same period for which regional-scale observations are available for comparison.

This study aims to verify the statistical-dynamical downscaling procedure. As in Frey-Buness et al. (1995) we apply the downscaling to the Alpine region. In order to obtain reliable results, the downscaling is

based on a decade of daily large-scale analyses in T42 resolution, which describes the present-day climate much more authentically than do results of a GCM control run.

The paper is organized as follows: In Section 2 the general concepts behind verifying the downscaling procedure are described and the large-scale input is discussed. The downscaled results are presented in Section 3 and compared with statistics for surface observations. Finally, in Section 4, conclusions are drawn from these results and a preview of future work is given.

2. VERIFICATION OF THE DOWNSCALING PROCEDURE

2.1. Observational data

A 10 yr set (1981 to 1990) of daily (00:00 h UTC) ECMWF analyses served as input to the statistical-dynamical downscaling procedure. The data are given in T42 resolution (approx. 250 km grid size) at 9 pressure levels from 1000 to 100 hPa. Fig. 1 shows the 12 boxes of the analysis grid which approximately cover the Alpine area and which are used for classification and evaluation of vertical profiles.

To verify the downscaled results we used surface observations in the Alpine region for the same decade.

A gridded mesoscale precipitation database based on a total of 3000 stations has only recently become available (Frei 1995, Frei et al. 1996). However, the density of stations used for this database is much higher in Germany, Austria and Switzerland than in the other countries of the greater Alpine region. Hence, the effective spatial resolution of the analytical procedure used for interpolating data to a grid is adapted to the local density of observations.

Unfortunately, gridded mesoscale datasets of wind and temperature covering the whole Alpine region are not yet available. Therefore, we selected 30 SYNOP (report of surface observation for a land station) stations which are distributed throughout the regional model domain. This dataset consists of 8 observations per day (except for a few stations that do not report during the night) in the same decade. Fig. 1 and Table 1 indicate the locations of the SYNOP stations used.

2.2. Large-scale weather types

The definition of large-scale weather types is an essential element of the statistical-dynamical downscaling procedure. Different approaches for the classification of large-scale fields are available (using threshold values, cluster analysis, etc.), the choice of an appropriate classification scheme depending on the specific requirements of the actual climate-impact problem.

This subsection describes the specific classification scheme used for a general verification of the procedure. It is based on the threshold method presented in Frey-Buness et al. (1995), and was further refined taking into account the experience gained in the earlier prototype study. For the application to the Alpine region we selected static stability, large-scale wind speed and wind direction as suitable parameters for the definition of large-scale weather types, as they determine the flow over or around mountains to a large extent.

Since static stability depends on season, we considered the stability effect by distinguishing between the winter half-year (more stable situations) and the summer half-year (less stable situations). Thus, as a first

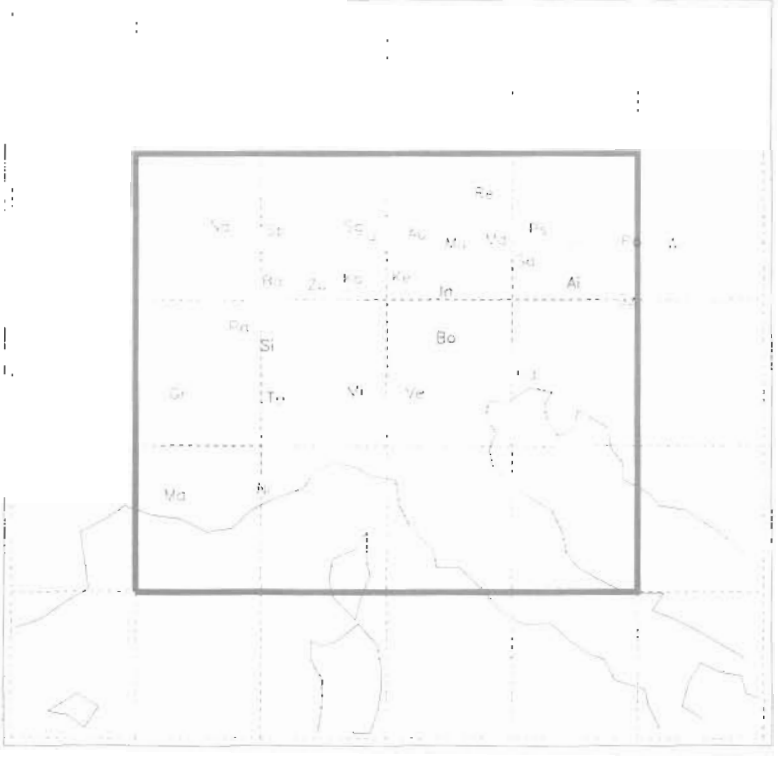

Fig. 1. The T42 grid for which the ECMWF analyses are available in the decade from 1981 to 1990. The box outlines the grid cells which approximately cover the regional model domain. Also shown are the locations of the 30 stations used for verification. The full names of the stations are given in Table 1

Table 1. Stations used for verification. Besides the stations' locations, their heights and corresponding model grid mesh heights are shown (in m above sea level). The last column gives the correlation coefficient between the observed and downscaled frequency distributions of near-surface wind direction. A: Austria; F: France; G: Germany; I: Italy; S: Switzerland

Station		Latitude (degree)	Longitude (degree)	Station height (m)	Model grid height (m)	Correlation coefficient
Na	Nancy (F)	48.4	6.1	217	396	0.21
Sb	Strasbourg (F)	48.3	7.4	154	141	0.37
Sg	Stuttgart (G)	48.4	9.1	419	332	0.48
Ul	Ulm (G)	48.2	9.6	523	531	0.41
Au	Augsburg (G)	48.3	10.6	463	456	0.35
Re	Regensburg (G)	49.0	12.1	371	392	0.17
Ps	Passau (G)	48.4	13.3	408	391	0.71
Ba	Bale-Mulehouse (F)	47.4	7.3	271	240	−0.18
Zu	Zürich/Kloten (S)	47.3	8.3	432	458	0.30
Ko	Konstanz (G)	47.4	9.1	447	514	0.60
Ke	Kempten (G)	47.4	10.2	705	738	0.43
Mu	München (G)	48.1	11.4	529	511	0.60
Md	Mühldorf (G)	48.2	12.3	402	459	0.34
Sa	Salzburg (A)	47.5	13.0	450	648	−0.19
Li	Linz (A)	48.1	14.1	313	335	0.34
Po	St. Pölten (A)	48.1	15.4	282	457	0.06
Wi	Wien (A)	48.1	16.3	190	274	0.49
Gz	Graz (A)	47.0	15.3	347	488	0.32
Pa	Payerne (S)	46.5	6.6	491	579	0.59
Gr	Grenoble (F)	45.2	5.2	386	274	−0.24
To	Torino (I)	45.1	7.4	287	579	0.00
Mi	Milano (I)	45.2	9.2	103	91	0.13
Ve	Verona (I)	45.2	10.5	68	61	0.08
Ud	Udine (I)	45.6	13.0	53	118	0.29
Si	Sion (S)	46.1	7.2	481	2011	−0.23
In	Innsbruck (A)	47.2	11.2	598	1427	−0.13
Ai	Aigen im Ennstal (A)	47.3	14.1	649	1372	−0.34
Bo	Bolzano (I)	46.3	11.2	241	937	−0.01
Ma	Marseille (F)	43.3	5.1	36	335	0.69
Ni	Nice (F)	43.4	7.1	10	0	−0.22

step we divided the large-scale time series into 2 subsets (summer and winter half-years, starting on 15 April and 15 October, respectively).

The stability effect was further taken into account in the next step, where we distinguished different types of large-scale precipitation. In Frey-Buness et al. (1995), stratiform and convective precipitation were not differentiated. Disregarding deep convection in the classification was assumed to be one reason for deficiencies found in the simulations, especially for summer. To account for this in the present study, we distinguished 3 types of large-scale precipitation: (1) days without precipitation ('fair weather'); (2) days with stratiform precipitation ('poor weather'); (3) days with convective precipitation ('shower weather').

In contrast to GCM results, the ECMWF analyses do not provide any information about the type of precipitation. Therefore, we used the SYNOP station data to group the daily large-scale analyses into the above-mentioned categories.

To define large-scale precipitation classes from local station data we computed the frequency distribution of daily precipitation events as a function of both regional extent and duration. The regional extent was measured by the number of stations observing precipitation (either stratiform or convective) on the specific day (max. 30 stations in the region). The duration was measured by how often these stations reported precipitation events (max. 8 observations per day). The resulting frequency distribution was bimodal. It showed one maximum for days with precipitation at 25 (of the 30) stations at 3 observing times and a second maximum for days with precipitation at only 2 or 3 stations at only 1 or 2 observing times (Heimann et al. 1994).

Regarding the gap in the bimodal distribution, days on which less than 8 stations recorded precipitation no more than 3 (4) times a day were assigned to the 'fair weather' type in the summer (winter) half-year. The remaining days were assigned to the 'poor weather' and 'shower weather' types depending on whether or not the number of stations reporting convective precipitation (shower, thunderstorms) at least 3 times a day exceeded 8.

Table 2. Frequencies (%) of the precipitation type groups for the ECMWF analyses (1981 to 1990)

	Fair weather days	Shower weather days	Poor weather days	Total
Winter	12	12	26	50
Summer	13	24	13	50
Total	25	36	39	100

The determined frequencies of the 3 precipitation types are presented in Table 2 for both seasons. Note that although local rain observations have been used to define large-scale precipitation types, the results of the downscaling procedure can still be compared with these observations, because the regional distribution of precipitation rates does not influence the definition of precipitation types, and it is the simulation of the regional distribution that we aim at with our downscaling procedure.

Each large-scale weather group was further subdivided according to the geostrophic wind speed and wind direction at the 850 hPa level. The geostrophic wind speed was deduced from the analyzed geopotential as an area mean of the centered differences at the 12 T42 grid cells (see Fig. 1). In contrast to the prototype study in Frey-Buness et al. (1995), the large-scale geostrophic wind speed was taken into account, since it is an essential parameter influencing orographically modified flows. We distinguished among calm, moderate and strong geostrophic wind velocity using 1 m s^{-1} and 6 m s^{-1} (8 m s^{-1}) as threshold values in the summer (winter) half-year. The threshold values accord with the frequency distribution that was found for each season (Fig. 2). Except for the calm class, we further distinguished among 12 uniform sectors (30° each) of geostrophic wind direction. A reduction in the total number of different large-scale weather types was achieved by combining the moderate and strong wind-speed classes in the case of 'fair weather', since high wind speeds are rather rare under this condition. Moreover, 2 strong wind-speed classes in the summer large-scale stratiform precipitation group contained less than 3 elements. These classes were combined with the moderate wind-speed classes.

A further reduction of weather types was attained by removing the discrimination between stratiform and convective precipitation for 5 easterly and southerly geostrophic wind directions in the winter half-year. This was justified due to the low frequency of these wind direction sectors for precipitation days in the winter half-year. Taking into account that 3 of the resulting classes were empty, we arrived at a total of 111 different weather types (see Fig. 3) on which the classification was based. 59 classes belonged to the summer half-year; the remaining 52 classes belonged to the winter half-year. The number of members per class (single days) varied between 3 and 129.

2.3. Regional simulations

The regional simulations were performed with a conventional 3-dimensional hydrostatic model that has already been used by Frey-Buness et al. (1995).

This model solves prognostic equations for the horizontal wind components, temperature, specific humidity, turbulent kinetic energy and the specific amounts of cloud droplets, cloud ice, rain drops and snow flakes. Diagnostic equations provide the vertical velocity, the Exner function and turbulent-diffusion coefficients for momentum, heat and moisture. Cloud processes are parameterized using an extended Kessler scheme (cf. Pielke 1984). The force-restore method proposed by Jacobsen & Heise (1982) is applied at the bottom boundary of the model. Short-

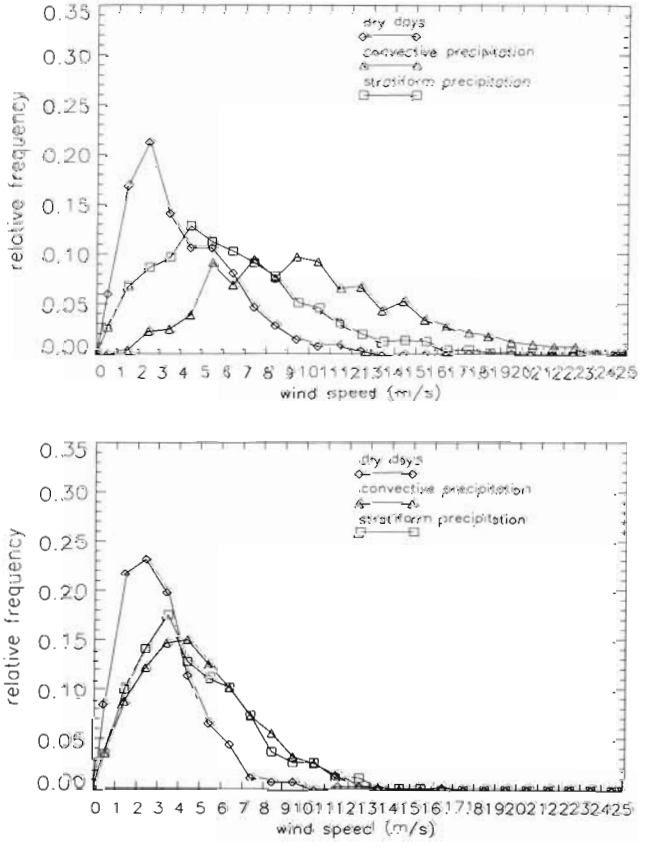

Fig. 2. Distribution of geostrophic wind speed at 850 hPa for the 3 precipitation types in winter (upper panel) and summer (lower panel) half-years, 1981 to 1990, averaged over the Alpine region

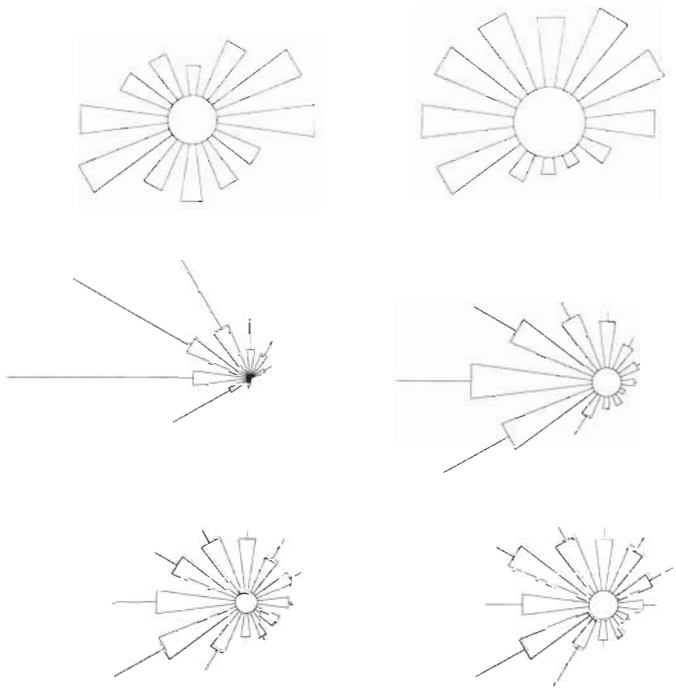

Fig. 3. Relative frequencies of the weather classes for each of the seasons (winter: left; summer: right) and precipitation type groups (dry days: top; convective precipitation: middle; stratiform precipitation: bottom). In each diagram the diameter of the circle is proportional to the relative frequency of the calm classes, whereas the lengths of the thick (thin) beams are proportional to the relative frequencies of the moderate (high) wind-speed classes in the wind directions (at 850 hPa) in which the beams point. The frequencies of the precipitation type groups are given in Table 2

wave and long-wave radiative energy transfer is considered as in Mahrer & Pielke (1977).

Appropriate values of roughness length, albedo, soil heat capacity and heat conductivity are specified for each of 5 different types of land-use: 'arable land', 'forests', 'urban areas', 'permanent snow cover/glaciers' and 'sea'. The initial values of land-surface temperature are taken from ECMWF analyses. They are corrected for elevation during the initialization procedure. Observed mean values are used for the sea-surface temperature.

Since the downscaling by Frey-Buness et al. (1995) suffered as a result of disregarding deep convection, an appropriate parameterization scheme is implemented following the mass-flux concept of Fritsch & Chappell (1980). In order to account for deep convective events, the upper boundary is elevated to 15 km above mean sea level. A detailed description of the model is given in Heimann (1990); its latest version is described in Heimann (1994).

The model domain encompasses the greater Alpine region with a horizontal resolution of 20 km (see Fig. 4). In the vertical, the model atmosphere is divided into 20 layers that follow the terrain and have a thickness increasing from 50 m near the ground to 1500 m below the model's top.

The regional model is not nested into a large-scale model. The simulations (1 for each weather type) are initialized with the mean vertical profiles of geostrophic wind, potential temperature and specific humidity, temporally averaged over the days belonging to the corresponding weather type and horizontally averaged over the 12 grid meshes covering the regional model domain.

The model is operated in the mesoscale mode with the Exner function representing the mesoscale deviation from the large-scale pressure field, which is determined by the vertical profile of the geostrophic wind.

A radiation boundary condition is used for the lateral boundaries with regard to the wind components, while a zero-gradient condition defines the lateral boundaries of temperature and humidity. The radiation boundary condition is used for wind and temperature at the upper boundary.

For the classes representing 'fair weather' we assume clear sky without precipitation: to allow for thermally induced diurnal circulation systems, the radiation and surface heat budget modules are activated and the corresponding simulations extend over a full diurnal cycle. Cloud physics parametrization is not activated. The model runs start with horizontally homogeneous fields. The topography is introduced during a 1 h diastrophism period. An additional 2 h are needed as spin-up time. After these 3 hours we simulate 24 hours and store the output every hour.

In addition, we assume overcast sky and large-scale lifting for the classes representing 'poor weather' and 'shower weather'. For these groups we integrate 8 hours, of which the first 4 hours are spin-up time. Precipitation is triggered in the model by prescribing an appropriate quantity of large-scale ascent (Frey-Buness 1993) as follows: a horizontally homogeneous but time-dependent vertical profile of vertical velocity is prescribed throughout the integration. During the first half hour of simulation, the maximum large-scale vertical velocity is fixed at a rather high value of 60 cm s^{-1} This triggers stratiform and, in case of sufficient potential instability, convective precipitation, without the influence of topography. By the end of the second hour, when the diastrophism starts, the maximum vertical velocity is reduced to 5 cm s^{-1}. Beginning with the fourth hour, the full orography is active. During the following 4 hours of simulation, the model results are stored hourly. These runs produce a steady precipitation rate in a stationary mesoscale flow field. This method is, of course, not able to provide absolute amounts of precipitation but it allows the determina-

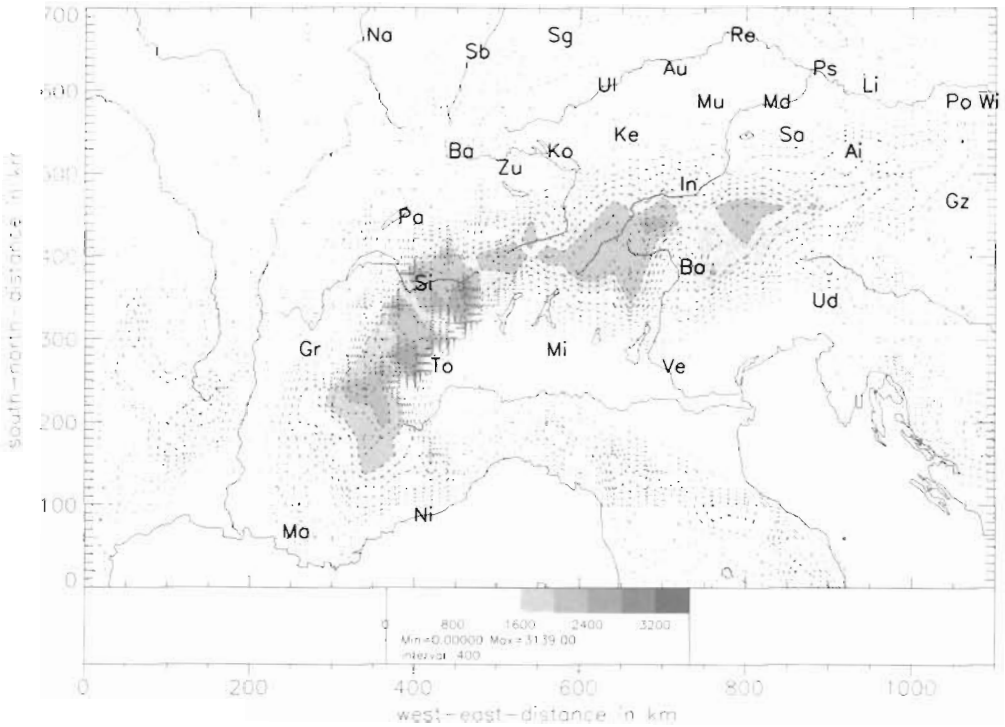

Fig. 4. Regional model domain showing the orography (in m) and major rivers. Dashed lines represent altitude intervals of 200 m. The abreviations denote the locations of 30 SYNOP stations used for verification (see Table 1 for full names of stations)

tion of regional patterns of precipitation rate (e.g. due to blocking and lee effects).

Admittedly, the reduction of the natural variety of cloudiness to only 2 categories, i.e. completely cloudy days and days without clouds, is a rather drastic simplification. Disregarding the diurnal cycle for the 'poor' and 'shower' weather classes results, of course, in a rough approximation, but it is nevertheless justified due to the considerable difference between 'fair weather' days on the one hand, and 'poor' or 'shower' weather days on the other, in the amplitude of the diurnal cycle of near surface temperature at the 30 SYNOP stations: the mean amplitude, averaged over 26 stations outside the inner-Alpine region, evaluated from 3-hour measurements, amounts to 8.2 K in the winter half-year and 12.1 K in the summer half-year for the fair weather group, while it is only 5.0 K for precipitation days in winter and 6.9 K (8.3 K) for shower (poor weather) days in summer.

2.4. Comparison of downscaled and observed values

Regional distributions of mean values of wind speed, temperature and precipitation as well as 2-dimensional fields of frequency distributions of wind direction (wind roses) were obtained by averaging the individual model results after weighting them with the corresponding frequencies of the respective large-scale weather types that were found for the decade 1981 to 1990.

The downscaled mean values of wind speed and temperature as well as the frequencies of wind direction were compared with the corresponding observed mean values and frequencies at the locations of the SYNOP stations. These comparisons were carried out using the downscaled values for the grid cell in which each respective station was located. Every verification of the output of numerical models with local observations has to cope with the problem of different spatial representativeness of the 2 datasets: the model results refer to a numerical grid volume (in our case 20 km × 20 km × 50 m), whereas the station measurements in general represent a much smaller space. Depending on the local influences to which the measuring equipment is exposed, the range of representation extends to some 100 to 1000 m. Therefore, one cannot expect a perfect agreement between observations and model data.

To give a quantitative measure of the quality of agreement between model results and observations, the mean absolute value of the error

$$\overline{|\Delta\varphi|} = \frac{1}{n}\sum_{i=1}^{n}\left|\varphi_{mod}^{(i)} - \varphi_{obs}^{(i)}\right|$$

(where φ denotes the climatological parameter of interest, and n the number of stations) is compared with the corresponding spatial standard deviation σ_{obs} of the local observations, which is a measure of the regional variation of the climatological variable. The results can be accepted if the mean absolute value of the error is considerably smaller than the observed spatial standard deviation. As a measure of the fraction of spatial variance of local measurements explained by model data, the relation $\sigma^2_{mod}/\sigma^2_{obs}$ (where σ denotes the spatial standard deviation) is computed for wind speed and temperature.

In the case of near-surface temperature, the downscaled results were additionally compared with the directly interpolated ECMWF analyses, in order to assess the improvement of the downscaling method over direct use of the large-scale field data.

To verify the downscaled precipitation, the regional distributions of accumulated precipitation, averaged over the winter and summer half-years from 1981 to 1990, were spatially standardized for both downscaled and observed fields, since only spatial variations of the downscaled precipitation can be interpreted, as mentioned before.

3. RESULTS OF VERIFICATION

The comparison of downscaled and observed values is discussed below for the selected parameters wind, temperature and precipitation. The downscaled regional distribution of mean values of all these parameters is shown. Comparisons are presented for each individual station in the case of wind and temperature. Where not explicitely stated otherwise, the inner-Alpine stations (Sion, Innsbruck, Aigen and Bolzano), which are all located in numerically unresolved deep valleys, are excluded from local comparison. Except for wind direction these comparisons are shown separately for the winter and summer half-years.

3.1. Wind

Fig. 5 shows the downscaled mean near-surface wind speed representing the decade 1981 to 1990. High values are generally found in mountainous regions and over the Tyrrhenian and Adriatic seas. Low-wind areas (less than 1.5 m s^{-1}) are situated near the borders of the Alps and the Apennines.

In Fig. 6 the resulting mean wind speeds at the station locations are compared with the observed ones.

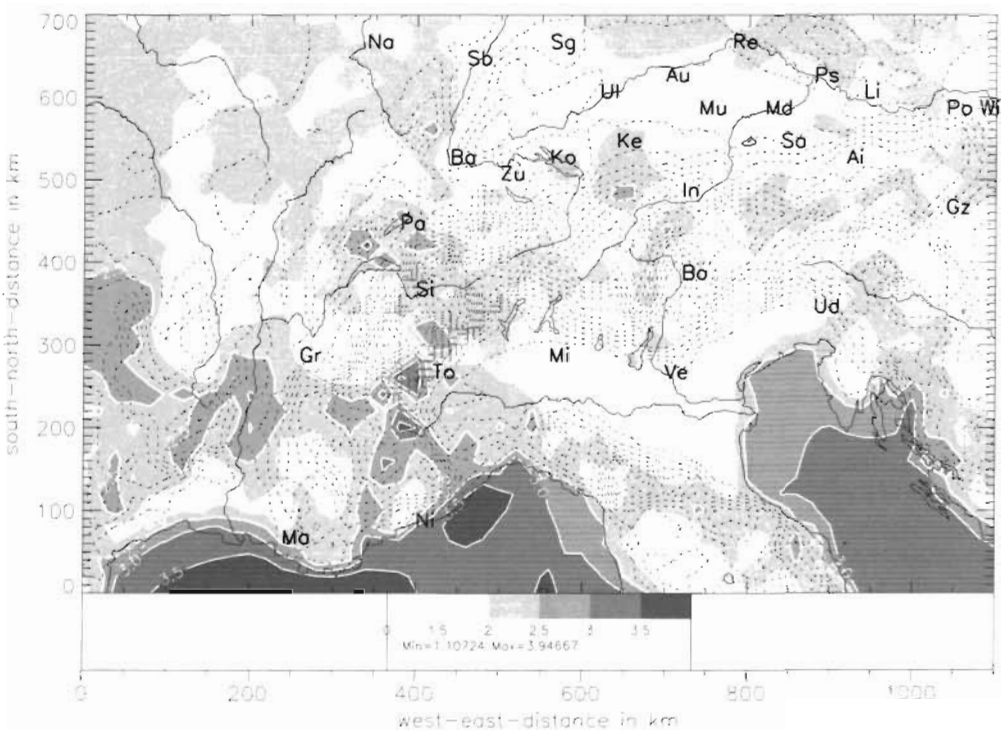

Fig. 5. Downscaled regional distribution of mean wind speed (in m s^{-1}) at 10 m above ground level, averaged over the whole decade 1981 to 1990

The quantitative results of the verification of this climatological variable are summarized in Table 3.

The first conclusion that can be drawn from these results is that only a fraction of the long-term climatic variability among the 26 stations is reproduced by the statistical-dynamical downscaling procedure. The fraction of variance explained by the model results, $\sigma^2_{mod.}/\sigma^2_{obs.}$, is 19% in winter and 12% in summer (see Table 3). As noted in the previous section, a complete reproduction of spatial variance could not be expected for wind speed distribution, because local influences on measurements contribute to the observed variance and cannot be resolved by a mesoscale model. Nevertheless, for the fair weather group in the summer half-year, a fraction of 37% is achieved, which shows that some improvement should be possible.

Fig. 6 also shows that for about half of the stations, the absolute value of the difference between the model grid value and the observation is larger than half of the observed spatial standard deviation. These differences are not satisfactory, because they are similar in magnitude to the spatial variance. Nevertheless, it is important to look at the local features of these stations where the downscaling seems to fail:

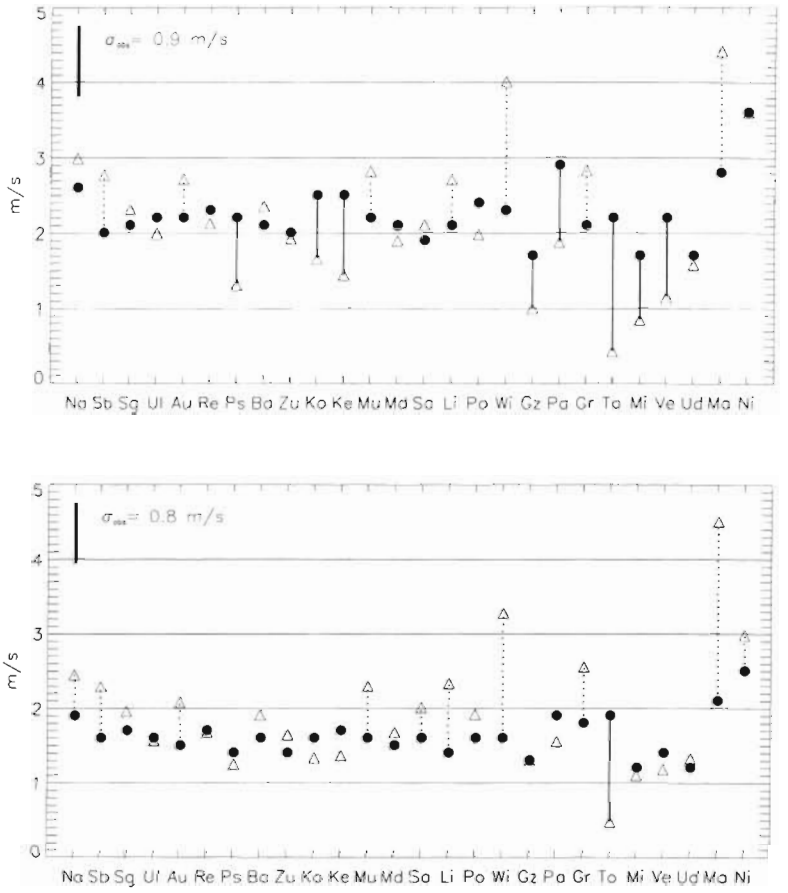

Fig. 6. Mean values of wind speed (10 m above ground level) at the location of 26 stations (see Table 1) for the winter (upper) and summer (lower) half-years, 1981 to 1990. (●) Model data; (△) observations. For overestimations larger than 0.5 $\sigma_{obs.}$, the corresponding values are linked with a solid line, for underestimations larger than 0.5 $\sigma_{obs.}$, with a broken line

The large error for Marseille might be partly due to the fact that the mean height of the corresponding model grid cell is 300 m above the station level and that the coastal effect is not elucidated. But note that the error vanishes when only fair weather days are taken into account for the comparison (not shown), and that for Marseille a daily amplitude of 2.0 m s^{-1} is observed for winter precipitation days, whereas the mean over the 26 stations is only 1.0 m s^{-1}. In summer, the observed amplitude

Table 3. Summary of verification results for wind speed (10 m above ground level); φ = wind speed, 10 m AGL; $\Delta\varphi = \varphi_{mod.} - \varphi_{obs.}$. Meaning of the columns, from left to right: mean relative error (averaged over the values at 26 locations), mean error, mean absolute value of the deviation between model grid result and observation (averaged over 26 stations), spatial standard deviation of the observed values, fraction of variance explained by the model results, and frequency of the corresponding weather type

	$\overline{\Delta\varphi/\varphi_{obs.}}$	$\overline{\Delta\varphi}$ (m s^{-1})	$\overline{\lvert\Delta\varphi\rvert}$ (m s^{-1})	$\sigma^2_{obs.}$ (m s^{-1})	$\sigma^2_{mod.}/\sigma^2_{obs.}$	Freq. (%)
Winter, poor/shower weather	0.27	0.1	0.8	1.0	0.22	38
Winter, fair weather	0.46	0.1	0.6	0.8	0.14	12
WINTER HALF-YEAR	0.29	0.1	0.7	0.9	0.19	50
Summer, shower weather	−0.09	−0.5	0.6	0.9	0.13	24
Summer, poor weather	0.00	−0.3	0.6	0.8	0.16	13
Summer, fair weather	0.32	0.0	0.5	0.6	0.37	13
SUMMER HALF-YEAR	0.01	−0.3	0.5	0.8	0.12	50

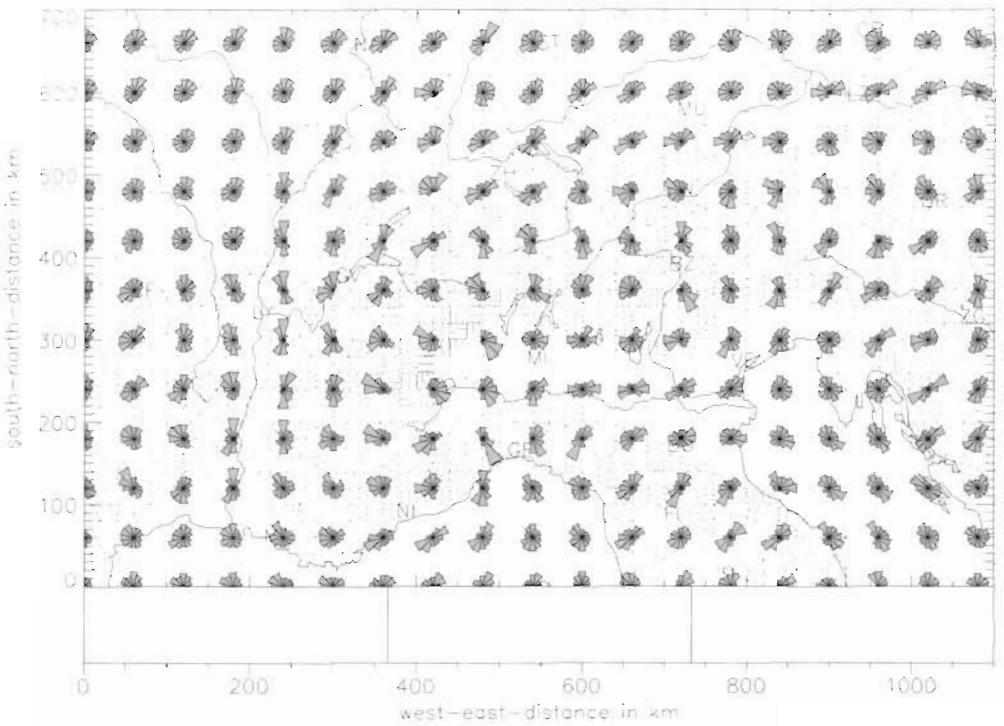

Fig. 7. Downscaled regional distribution of wind direction frequencies at 10 m above ground level for all weather types, 1981 to 1990. The frequencies of the 30° sectors are proportional to the area of the beams in the respective sectors. To improve readability, only the distributions at every third grid mesh are shown

amounts to 3.7 m s^{-1} for shower days and 3.1 m s^{-1} for poor weather days, with mean values of 1.8 and 1.6 m s^{-1}, respectively. Thus, our disregarding of the diurnal cycle for precipitation days could be an error source for this location. It should be mentioned that the good agreement for the mean wind speed in Nice occurs because an overestimation for the simulations corresponding to precipitation days and an underestimation for the fair-weather-type simulation compensate for each other.

Some stations in the Po Valley, namely Torino, Milano, and Verona, report wind speeds less than 0.5 m s^{-1} in 85, 70 and 50%, respectively, of the time during the winter half-year. The Po Valley is known for long periods of fog in winter which are often accompanied by surface-based inversion layers, in which the air is decoupled from the flow above and is often stagnant. The development of these surface inversions cannot be reproduced by our method, and thus it overestimates the wind speed in the Po Valley in winter. The overestimation is highest for Torino, where it is even found in the summer half-year, when the rest of the Po Valley observations are reproduced quite well. This might be due to the very steep orography near Torino, which is smoothed by the 20 km grid of the model.

The overestimation of wind speed in the winter half-year for some other stations (Passau, Konstanz, Kempten, Graz and Payerne) does not appear in the summer half-year. Again, this points to an underrepresentation of stagnant air close to the surface. Apart from the stations discussed separately above, the model shows a general tendency to underestimate wind speed (by about 0.5 m s^{-1}). In the summer half-year, this feature is reflected in the mean deviation of −0.3 m s^{-1} (see Table 3), which indicates a systematic error. The fact that this underestimation does generally not appear for the fair weather group (not shown) indicates that disregarding the diurnal cycle is a possible reason.

The extreme underestimation of wind speed in Wien (which appears in all weather groups) is probably due to the fact that this situation was close to the lateral boundary of the regional model domain. The mean absolute value of the deviation between model results and station data is 0.7 m s^{-1} in winter and 0.5 m s^{-1} in summer (see Table 3), corresponding to a fraction of about 0.7 of the observed spatial standard deviations (1.0 and 0.8 m s^{-1}, respectively). The effect of topography on the wind field is also elucidated by the regional distribution of wind roses representing the frequency distributions of the surface wind direction at 10 m above ground (Fig. 7). A strong channeling of the airflow, characterized by bimodal distributions of wind direction, is apparent along major valleys (e.g. Rhone

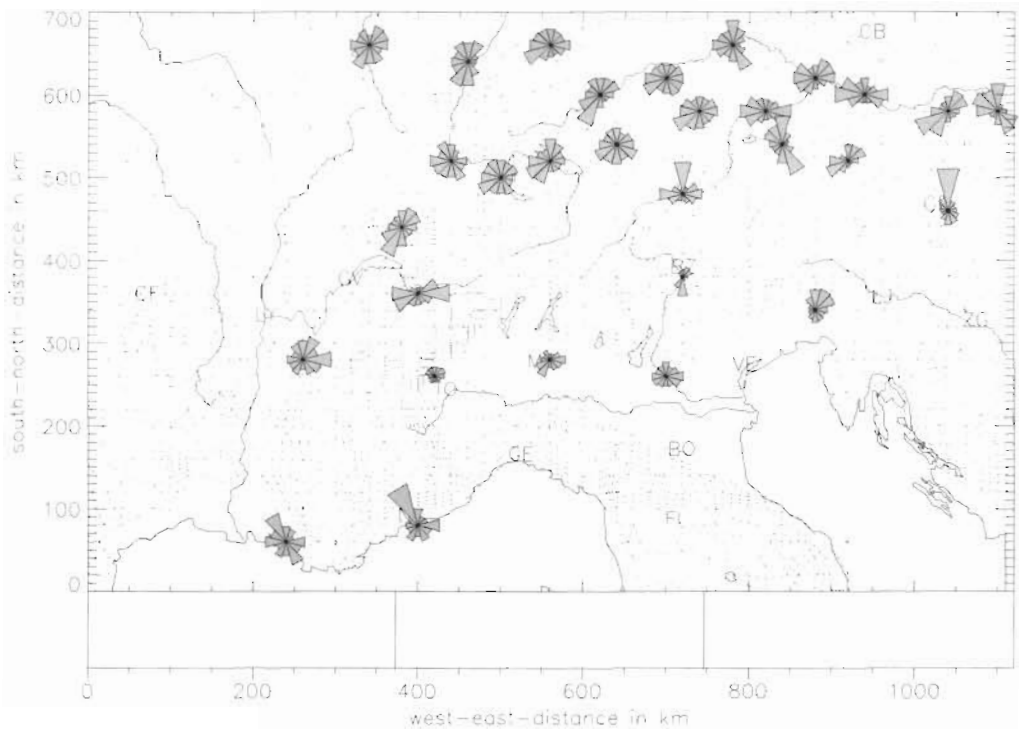

Fig. 8. Observed frequency distributions of wind direction at 10 m above ground level, 1981 to 1990. The frequencies of the 30° sectors are proportional to the area of the beams in the respective sectors. The differences between the total areas of the wind roses result from different frequencies of calm wind situations (wind speed less than 0.5 m s^{-1})

Valley, Danube Valley), but also above the Adriatic Sea.

The observed frequency distributions of wind direction for the 30 stations are shown in Fig. 8.

The station-wise comparison of model data with observations does not yield a completely satisfactory agreement with respect to the wind direction distributions. One has to bear in mind that wind direction strongly depends on local features on a scale which is not resolved by the model. Nevertheless, some features are well represented in the model: the channeling along the Danube Valley, and the dominance of northwesterly winds in Marseille and of southwesterly winds in the region of Payerne. At Graz, the increased frequency of northerly winds is captured, but to a lower degree.

As a quantitative measure of the quality of fit, Table 1 shows the correlation coefficients between the observed and downscaled frequency distributions of wind direction at the various station locations. Fig. 9 shows the frequency distributions of the computed and observed wind direction for selected stations. This selection of stations is intended to show the range of possible performances, with examples of good as well as poor agreement. The results are satisfactory for stations like Payerne, Ulm and Passau (with correlation coefficients of 0.59, 0.41 and 0.71, respectively), and also for Marseille (correlation coefficient 0.69) (except for one observed wind-direction maximum at 150° which is not reproduced by the model). Nice and Grenoble (with correlation coefficients of −0.22 and −0.24, respectively) are examples of stations with large discrepancies. In Nice, the failure of the downscaling procedure is probably caused by the narrow side-valley of the Var River which is not resolved by the numerical grid, but which gives rise to frequent northerly drainage flow situations. Similarly, in Grenoble the observed maximum at 90° (east wind) is probably caused by the opening of the Isere Valley, which is also not resolved by the model topography.

3.2. Temperature

Fig. 10 shows the mean temperature field at 2 m above ground for the whole 10 yr period. The regional variance in near-surface temperature results to a considerable extent from the dependency of temperature on terrain elevation. Therefore, the temperature values have been reduced to their corresponding values at mean sea level (assuming a vertical lapse rate of 6.5 K km^{-1}) for comparison of model grid values with station data. In addition to this comparison, the downscaled results are also compared with those from the directly

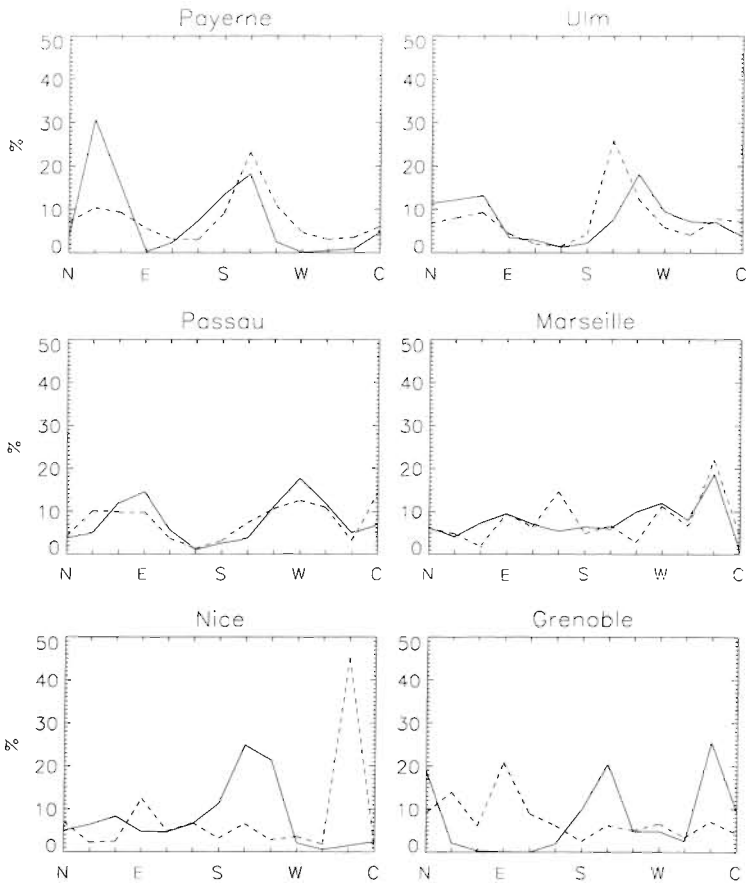

Fig. 9. Computed (solid lines) and observed (dashed lines) frequency distributions of wind direction at 10 m above ground level 1981 to 1990, at selected stations. C: calm. See Table 1 for correlation coefficients

interpolated large-scale field (derived by interpolating the T42 grid values of temperature at 1000 hPa to the locations of the stations after reduction to mean sea level).

Several sources of systematic deviations between measured and simulated mean temperatures are possible:

Error 1: a systematic bias of the interpolated large-scale analyses (at 00:00 h UTC) relative to the measurements (at 00:00 h UTC);

Error 2: the neglecting of the diurnal cycle for the wet ('poor' and 'shower') weather types;

Error 3: a possible erroneous calculation of the diurnal cycle.

Error 1 is assessed by comparing the analysed temperature at 00:00 h UTC with the corresponding measurements at 00:00 h UTC. This shows a positive bias for all weather types except for 'fair weather' days in summer.

Error 2 always leads to a negative deviation, since the time of initialization (00:00 h UTC) represents a nocturnal temperature below the daily mean. This is especially true in summer, where the daily temperature amplitude is more pronounced.

Error 3 would lead to positive or negative deviations for the 'fair weather' days.

Table 4 summarizes this error assessment and indicates the sign of the systematic errors found by direct comparison of downscaled and observed mean temperatures (see also Table 5 and Fig. 11).

From the net errors found for 'fair weather' days in summer, we presume that Error 3 is negligible. For 'poor' and 'shower' weather in winter, Errors 1 and 2 compensate for each other, while in summer, Error 2 dominates and results in a negative net deviation. As 'fair weather' constitutes only one quarter of all the days in a season, the deviations of the 'poor' and 'shower' weather type contribute more to the overall systematic error.

Apart from the systematic errors discussed above, the regional distribution of temperature which remains after reduction to mean sea level is fairly well reproduced. The fraction of variance explained by the model results is even >1 (see Table 5), due to an overestimation of the north-south gradient. The interpolated analyses also yield a fraction of variance >1 in winter, while in summer the spatial variance of the interpolated large-scale field is the same as that between the station observations.

It should be mentioned that the deviations for Ulm, Kempten and St. Pölten are due to missing measurements during nighttime at these stations, which leads

Table 4. Expected sign of the systematic deviation of the simulated mean near-surface temperature from the observed one, due to different possible errors (see text), and signs of the resulting systematic deviations between downscaled and observed mean temperature. Doubled signs indicate strong deviations, signs in parentheses indicate weak deviations

	Winter		Summer	
	Dry days	Wet days	Dry days	Wet days
Error 1	+	+	0	+
Error 2	0	–	0	– –
Error 3	+/–	0	+/–	0
Comparison of downscaled and observed values	+ (+)	0	0 –	–

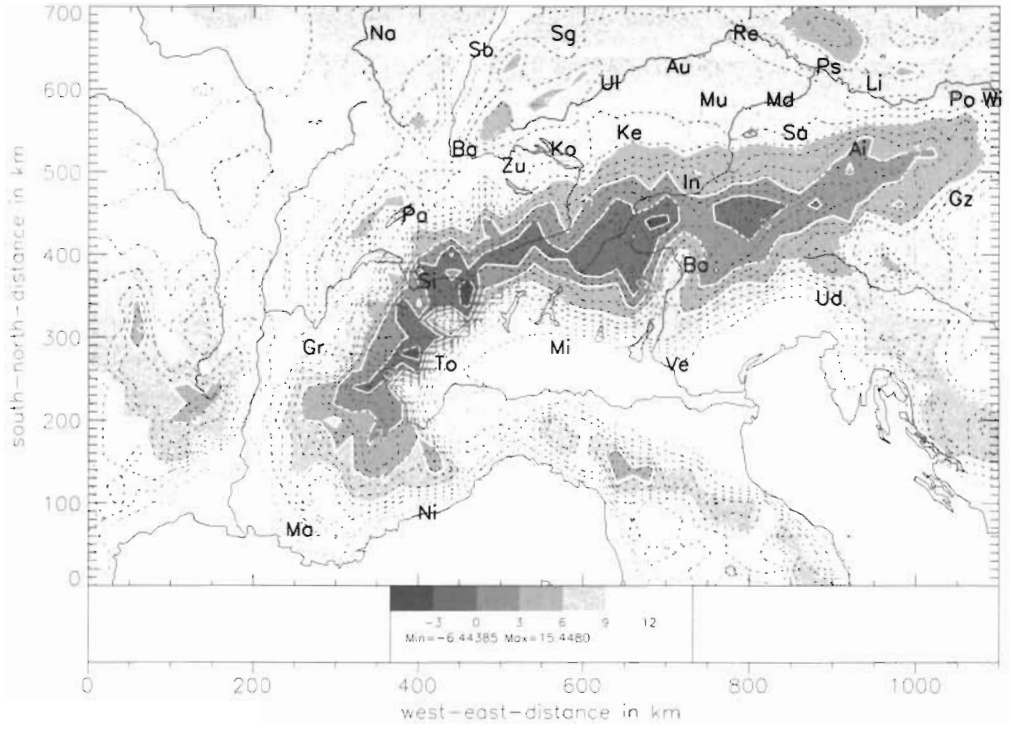

Fig. 10. Regional distribution of mean temperature (°C) at 2 m above ground level, 1981 to 1990

to an overestimation of observed daily mean values in summer.

In summary, the results for near-surface temperature show that the statistical-dynamical downscaling method is able to reproduce the observed temperature features in winter. Both absolute values and the regional variability are well reproduced. In this season, the downscaled results lead to an improved representation of temperature variables at the stations, compared with the interpolated large-scale fields on which the downscaling is based. In summer, only fair-weather-type situations are well captured. For the other weather types, neglecting the diurnal cycle leads to a systematic underestimation of the mean temperature in this season.

3.3. Precipitation

The resulting fields of mean precipitation are shown in Fig. 12 (winter half-year) and Fig. 13 (summer half-year). As absolute values of mean precipitation per day cannot be directly interpreted and compared with observations, the downscaled regional precipitation

Table 5. Summary of verification results for near-surface temperature, reduced to mean sea level; φ = temperature at mean sea level MSL; $\Delta\varphi = \varphi_{mod} - \varphi_{obs.}$ (or $\Delta\varphi = \varphi_{ana.} - \varphi_{obs.}$). See Table 3 for explanation of column headings. Values in parentheses give the corresponding values for the directly interpolated large-scale analyses

	$\overline{\Delta\varphi/\varphi_{obs}}$	$\overline{\Delta\varphi}$ (K)	$\overline{\lvert\Delta\varphi\rvert}$ (K)	$\sigma_{obs.}$ (K)	$\sigma^2_{mod.}/\sigma^2_{obs.}$ ($\sigma^2_{ana.}/\sigma^2_{obs.}$)	Freq. (%)
Winter, poor/shower weather	0.02 (0.17)	0.1 (0.8)	0.8 (1.5)	1.4	1.5 (0.9)	38
Winter, fair weather	0.33 (0.48)	1.8 (2.2)	1.8 (2.9)	1.9	1.0 (0.7)	12
WINTER HALF-YEAR	0.09 (0.28)	0.5 (1.6)	0.8 (1.6)	1.5	1.3 (1.5)	50
Summer, shower weather	−0.10 (−0.02)	−1.8 (−0.3)	1.8 (0.6)	1.2	1.5 (0.8)	24
Summer, poor weather	−0.11 (−0.04)	−1.8 (−0.7)	1.8 (0.8)	1.1	1.4 (0.9)	13
Summer, fair weather	0.00 (0.00)	0.0 (0.0)	0.7 (0.7)	1.3	1.3 (1.5)	13
SUMMER HALF-YEAR	−0.07 (0.02)	−1.3 (0.3)	1.3 (0.6)	1.2	1.3 (1.0)	50

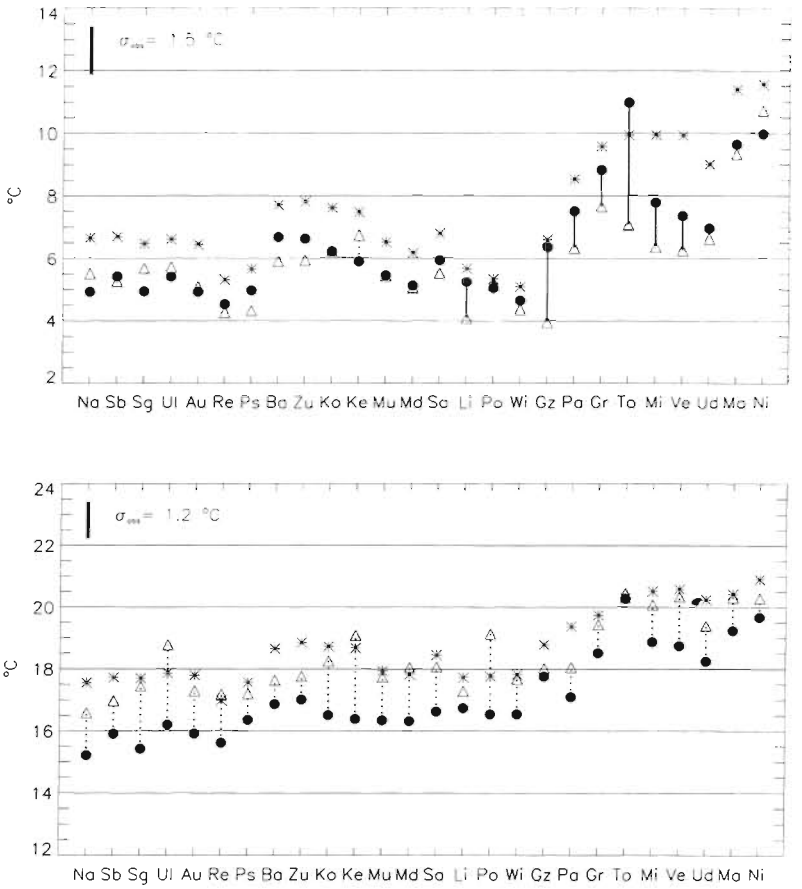

Fig. 11. Mean values of temperature, reduced to mean sea level, at the location of 26 stations (see Table 1) for the winter (upper) and summer (lower) half-years, 1981 to 1990. (●) Model data; (△) observations; (·) interpolated large-scale analyses. See Fig. 6 for further explanations

distribution $r(x,y)$ (accumulated precipitation, averaged over the corresponding model runs) was standardized, i.e. transformed to a distribution $r_s(x,y) = [r(x,y) - \overline{r(x,y)}]/\sigma$, where σ denotes the spatial standard deviation of the distribution $r(x,y)$.

The spatial average $\overline{r(x,y)}$ amounts to 0.6 mm in winter and 0.7 mm in summer The spatial standard deviation is 0.7 mm in winter and 0.5 mm in summer. The standardized distributions have a mean value of $\overline{r_s} = \overline{r_s(x,y)} = 0$ and a regional variance $\sigma^2(r_s) = 1$.

Figs. 14 & 15 show the corresponding observed precipitation distributions for the winter and summer half-year, respectively, from 1981 to 1990. The fields have been spatially standardized in the same way as the downscaled precipitation. Note that, for both downscaled and observed precipitation fields, only the subarea of the model domain for which observations were available (i.e. over land) was used for standardization.

The corresponding spatial average of the observed precipitation distribution amounts to 2.3 mm d^{-1} in winter and 2.8 mm d^{-1} in summer, while the spatial standard deviation is 0.8 mm d^{-1} in winter and 1.0 mm d^{-1} in summer.

A prominent feature of the observed precipitation distribution is the occurrence of relatively dry zones along the main crest of the Alps, surrounded by relatively wet zones to the north and south. This feature is not reproduced by the downscaled precipitation, where the precipitation is in general more strongly correlated with altitude.

In the winter half-year, the observed precipitation shows maxima in the northwestern Alps which are only partly reproduced in the downscaled field. The high precipitation in the Ticino region (western Alps) and the Mont Blanc region is also found in the downscaled field, where a broad region of high precipitation extends over the high-altitude region in the western Alps.

The observed maxima in the Apennines, the Swiss Jura mountains and the Black Forest are also present in the downscaled precipitation, although they are not as pronounced as the inner Alpine maxima. The same holds for the minima observed in the Venosta Valley and the lower Po Valley. The minimum in the upper Po Valley is not reproduced. The relatively low precipitation observed in the upper Rhine Valley as well as in the Danube Valley is also found in the downscaled field.

In the summer half-year, the observed precipitation shows maxima in the north and northeast of the Alps as well as in the Ticino region and the Friuli region (southeast rim of the Alps). Only the maximum in the Ticino region is reproduced in the downscaled precipitation field, where a broad region of high precipitation is found, similarly to the winter half-year results. Low precipitation is observed and modelled in the lower Rhone Valley and lower Po Valley, but the minima near Marseille and Nice are not reproduced. Moderately low precipitation rates are observed and modelled in the Danube Valley, as in the winter half-year.

Thus, neither summer nor winter half-year precipitation is satisfactorily reproduced by the downscaling procedure in its present setup. The results are worse for the summer half-year, where convective precipitation is more important.

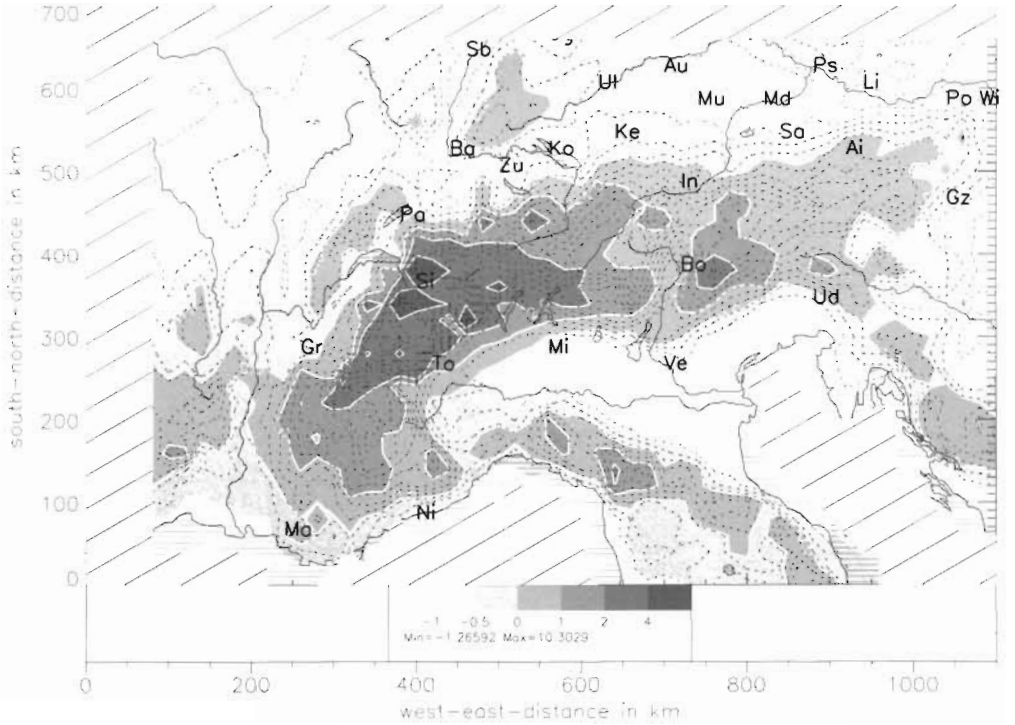

Fig. 12. Downscaled regional distribution of mean daily precipitation, winter half-year 1981 to 1990, standardized. Areas where no observations were available are hatched. They were not considered for standardization

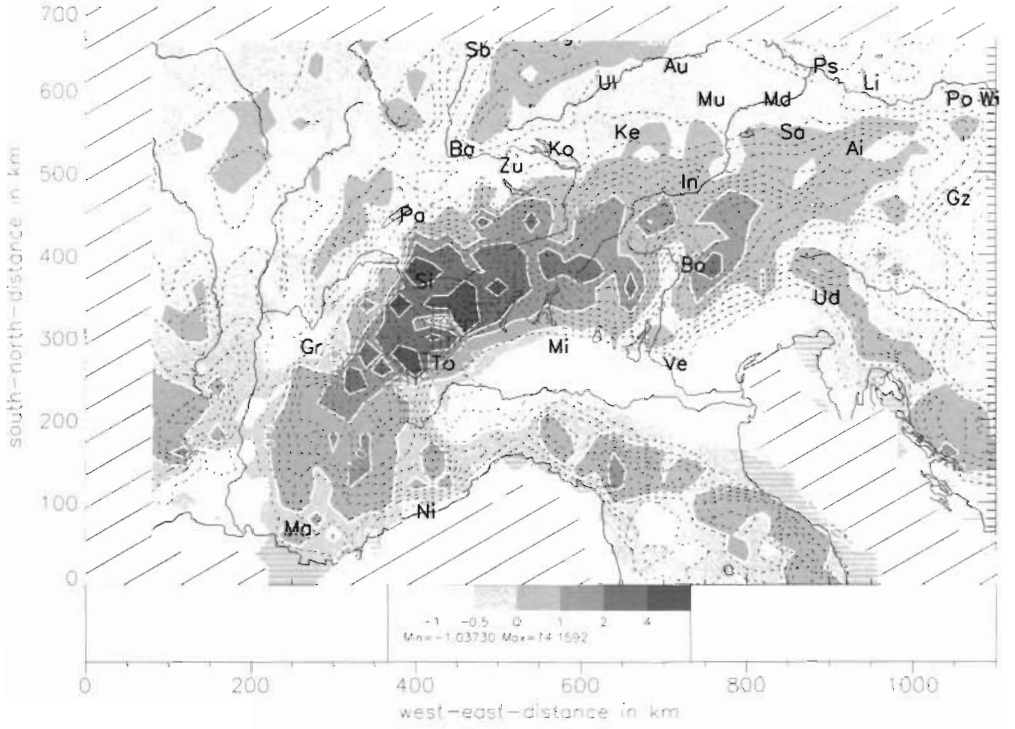

Fig. 13. Downscaled regional distribution of mean daily precipitation, summer half-year 1981 to 1990, standardized

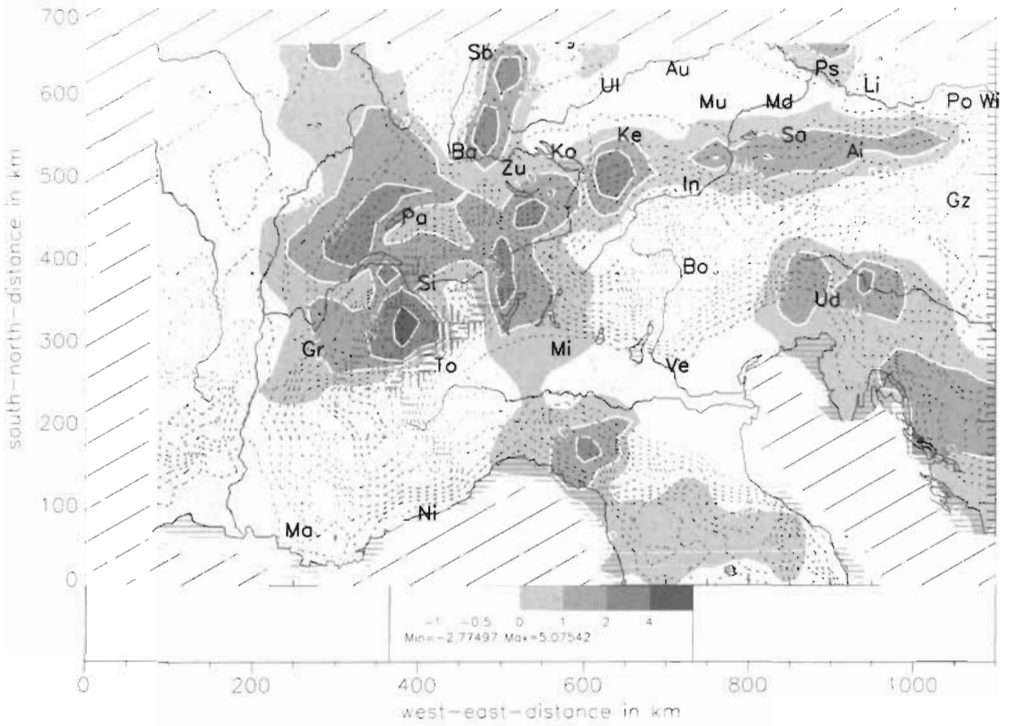

Fig. 14 Observed regional distribution of mean daily precipitation, winter half-year 1981 to 1990, standardized

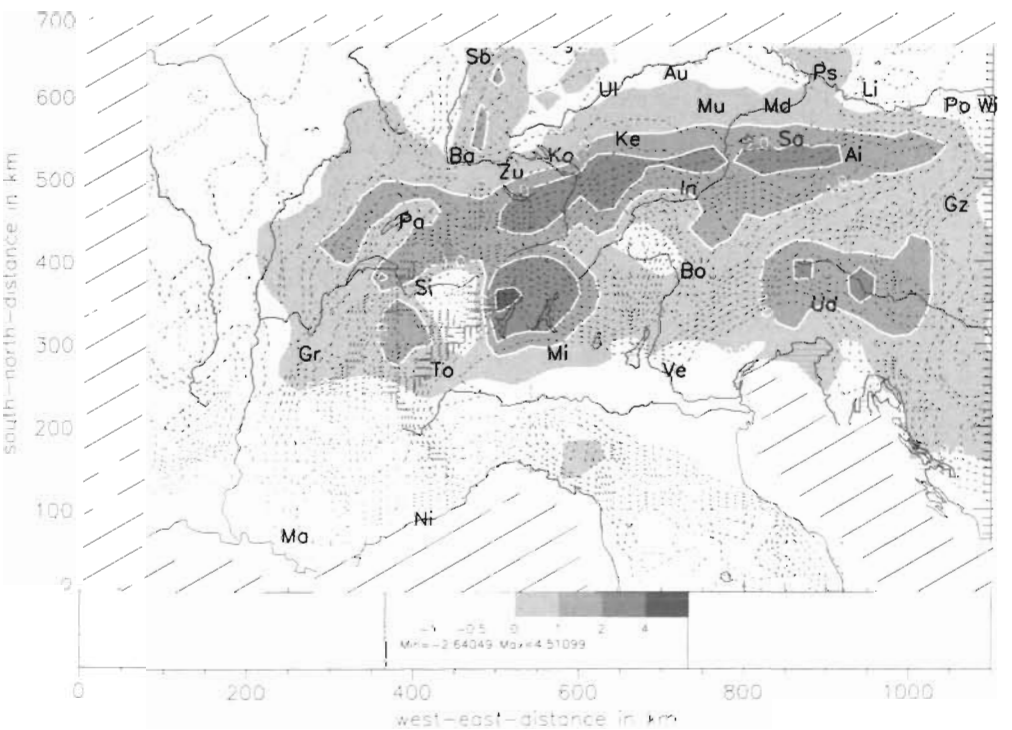

Fig. 15. Observed regional distribution of mean daily precipitation, summer half-year 1981 to 1990, standardized

4. CONCLUSIONS AND PERSPECTIVES

In summary, the results of the verification study show that the downscaling procedure reproduces some features of the observed wind and temperature variables near the ground on horizontal scales ranging from 100 to 1000 km. To some extent, the deviations of station data from corresponding model grid results can be explained by the influence of subgrid-scale features on the local observations. This especially applies to the local frequency distributions of near-surface wind direction.

Systematic errors occur due to a bias of the large-scale analyses at 00:00 h UTC (the time used to initialize the simulations) relative to the local observations at 00:00 h UTC, and due to neglecting the diurnal cycle for the wet (i.e. 'poor' and 'shower') weather types. This is especially true for the systematic underestimation of temperature and wind speed in summer. In future applications, the daily cycle should definitely be considered.

The remaining discrepancies, especially concerning the downscaled precipitation distribution and the reduced spatial variability of the simulated mean near-surface wind speed distribution, seem to confirm Egger's (1995) findings that the restriction to stationary and horizontally homogeneous large-scale fields as basic states of the regional simulations is crucial. In the case of the Alps, transient disturbances such as lee cyclogenes and propagating fronts are important factors of the regional climate.

The problem is avoided as long as statistical-dynamical downscaling in its present setup is applied to specific climate aspects for which transient disturbances are of minor importance. In addition, such a specialization allows the classification scheme to be more accurately adapted to the problem of interest.

Current applications of the statistical-dynamical downscaling method corroborate this assumption. Heimann (1996) adapted the statistical-dynamical downscaling procedure in a diagnostic climate study to steady-state 'foehn' situations (southerly to southwesterly flow across the Alps) and obtained reasonable results with respect to the regional wind-field climatology. Preliminary results of Sept et al. (1995) show that major improvements can be obtained when the classification into large-scale weather types is adapted to specific regional events: In order to estimate the frequency of thunderstorms in southern Bavaria, they chose a classification scheme that distinguished among different stability groups. Moreover, the simulations were designed to enable different mechanisms which could trigger deep convection. Finally, the diurnal cycle was considered for situations favouring thunderstorm release through heating of the boundary layer. The resulting summertime precipitation pattern agreed well with the corresponding observations.

Further amendments of the statistical-dynamical downscaling, which allow application of the method to phenomena for which transient disturbances are relevant, are under consideration. Instead of defining weather types by threshold values and using spatially averaged vertical profiles of large-scale parameters to initialize the regional model, it is possible for large-scale fields to be classified and coordinated to representative patterns by means of cluster analysis. Such patterns, when used as inhomogeneous initial states and time-dependent large-scale boundary conditions of the regional simulations, would permit the generation and propagation of transient disturbances. In this case, the regional model would simulate episodes of several days' duration, during which these disturbances would cross the regional domain. Although statistical-dynamical downscaling of episodes will work similarly to dynamical downscaling, the total number of simulated days will be significantly lower due to the combination of similar large-scale situations into clusters.

Thus, statistical-dynamical downscaling remains an efficient alternative for diagnostic climate studies and regional climate scenario assessments.

Acknowledgements. This study was partly sponsored by the European Commission under contract EV5V-CT92-0126. The ECMWF analyses were provided by the Deutsches Klimarechenzentrum (DKRZ). The SYNOP station data were made available by the Deutscher Wetterdienst (DWD). We thank Vladimir Sept, who processed the SYNOP data and contributed helpful comments, and Christoph Frei, who made available the gridded precipitation climatology of the Alpine region. The comments and suggestions of 3 anonymous referees are gratefully acknowledged.

LITERATURE CITED

Déqué M, Piedelievre JP (1995) High resolution climate simulation over Europe. Clim Dyn 11:321–339

Egger J (1995) Regional statistical-dynamical climate modeling: tests. Beitr Phys Atm 68:281–289

Frei C (1995) An Alpine precipitation climatology based on high-resolution rain-gauge observations. MAP Newsl 3: 46–47 (obtainable from Schweizerische Meteorologische Anstalt, Krähbühlstr 58, CH-8044 Zürich, Switzerland)

Frei C, Widmann M, Schär C (1996) Precipitation climate of the European Alps as deduced from high-resolution rainguage observations. Int J Climatol (in press)

Frey-Buness A (1993) Ein statistisch-dynamisches Verfahren zur Regionalisierung globaler Klimasimulationen. DLR Forschungsbericht 93–47 (obtainable from DLR, Zentrale Allgemeine Dienste, Versand, D-51140 Köln, Germany)

Frey-Buness A, Heimann D, Sausen R (1995) A statistical-dynamical downscaling procedure for global climate simulations. Theor Appl Climatol 50:117–131

Fritsch JM, Chappell CF (1980) Numerical prediction of convectively driven mesoscale pressure systems. Part I: convective parameterization. J Atmos Sci 37:1722–1733

Giorgi F (1990) Simulation of regional climate using a limited area model nested in a general circulation model. J Clim 3: 941–963

Giorgi F, Shields Brodeur C, Bates GT (1994) Regional climate change scenarios over the United States produced with a nested regional climate model. J Clim 7:375–399

Heimann D (1990) Three-dimensional modeling of cold fronts approaching the Alps including latent heat effects. Meteor Atmos Phys 42:197–219

Heimann D (1994) REWIH3D-1.0: Modell- und Programmbeschreibung. Rep 3, DLR, Institut für Physik der Atmosphäre, Oberpfaffenhofen

Heimann D (1996) Mesoscale wind characteristics and potential gravity-wave formation during cross-Alpine flow. Meteorol Atmos Phys (in press)

Heimann D, Sept V, Fuentes D (1994) The frequency of convective storms north of the Alps as a function of the large-scale climate. Ann Meteorol 30:21–24

Jacobsen I, Heise E (1982) A new economic method for the computation of the surface temperature in numerical models. Beitr Phys Atm 55:128–141

Jones RG, Murphy JM, Noguer M (1995) Simulation of climate change over Europe using a nested regional climate model. Part I. Assessment of control climate including sensitivity to location of lateral boundaries. Q J R Meterol Soc 121:1413–1449

Mahrer Y, Pielke RA (1977) A numerical study of airflow over irregular terrain. Beitr Phys Atm 50:98–113

Pielke RA (1984) Mesoscale meteorological modeling. Academic Press, New York

Roeckner E, Arpe K, Bengtsson L, Brinkop S, Dümenil L, Kirk E, Lunkeit F, Esch M, Ponater M, Rockel B, Sausen R, Schlese U, Schubert S, Windelband M (1992) Simulation of the present-day climate with the ECHAM model: impact of model physics and resolution. Rep No. 93, Max-Planck-Institut für Meteorologie, Hamburg

Sept V, Fuentes U, Heimann D, Sausen R (1995) Estimating the thunderstorm frequency north of the Alps by means of statistical-dynamical downscaling. MAP Newsl 3:71–72 (obtainable from Schweizerische Meteorologische Anstalt, Krähbühlstr 58, CH-8044 Zürich, Switzerland)

von Storch H, Zorita E, Cubasch U (1993) Downscaling of global climate change estimates to regional scales: an application to Iberian rainfall in wintertime. J Clim 6: 1161–1171

Zorita E, Hughes J, Lettenmaier D, von Storch H (1995) Stochastic characterization of regional circulation patterns for climate model diagnosis and estimation of local precipitation. J Clim 8:1023–1042

Editor: H. von Storch, Geesthacht, Germany

Manuscript first received: December 16, 1995
Revised version accepted: August 2, 1996